Research Square

Preprints are preliminary reports that have not undergone peer review.
They should not be considered conclusive, used to inform clinical practice,
or referenced by the media as validated information.

Cholinergic Nerve-Driven B-Cell Metabolic Reprogramming Suppresses CD8+ T Cell Cytotoxicity in Gastric Cancer via MEK/ERK-OXPHOS

Hankun Hao

haohankun@163.com

Huashan Hospital Fudan University

Mingye Ma

Huashan Hospital Fudan University

Zeqin Wang

Huashan Hospital Fudan University

Jun Hong

Huashan Hospital Fudan University

Jian Wang

Huashan Hospital Fudan University

Zihao Wang

Huashan Hospital Fudan University

Wenliang Cui

Huashan Hospital Fudan University

Yanming Zhang

Huashan Hospital Fudan University

Wenweiran Li

Shanghai Fifth People's Hospital, Fudan University

Xinzhu Li

Huashan Hospital Fudan University

Jiayue Zheng

Huashan Hospital Fudan University

Xiangxi Ye

Huashan Hospital Fudan University

Qi Zhou

Huashan Hospital Fudan University

Kaiyi Fu

Huashan Hospital Fudan University

Maolin Ye
Huashan Hospital Fudan University
Lingxi Lin
Huashan Hospital Fudan University
Yuting He
Huashan Hospital Fudan University
Xiaoxuan Su
Fudan University
Lishuang Lin
Fudan University
Yaping Wang
Huashan Hospital Fudan University
Feifei Luo
Huashan Hospital Fudan University https://orcid.org/0000-0002-3834-0188

Article

Keywords:

Posted Date: November 17th, 2026

DOI: https://doi.org/10.21203/rs.3.rs-10784606/v1

License: This work is licensed under a Creative Commons Attribution 4.0 International License.
Read Full License

Additional Declarations:
There is **NO** Competing Interest.

Table 1 is available in the Supplementary Files section.

TITLE PAGE

Cholinergic Nerve-Driven B-Cell Metabolic Reprogramming Suppresses CD8⁺ T Cell Cytotoxicity in Gastric Cancer via MEK/ERK-OXPHOS

Mingye Ma[1,#], Zeqin Wang[1,#], Jun Hong[1,#], Jian Wang[1], Zihao Wang[1], Wenliang Cui[1], Yanming Zhang[2], Wenweiran Li[3], Xinzhu Li[2], Jiayue Zheng[2], Xiangxi Ye[2], Qi Zhou[2], Kaiyi Fu[2], Maolin Ye[2], Lingxi Lin[2], Yuting He[2], Xiaoxuan Su[4], Lishuang Lin[5], Yaping Wang[1,*], Feifei Luo[2,*], Hankun Hao[1,*]

[1]Division of Gastrointestinal Surgery, Department of General Surgery, Huashan Hospital, Fudan University, Shanghai 200040, China

[2]Department of Digestive Diseases, and National Clinical Research Center for Aging and Medicine, Huashan Hospital, Fudan University, Shanghai 200040, China

[3]Department of Trauma-Emergency & Critical Care Medicine, Shanghai Fifth People's Hospital, Fudan University, 128 Ruili Road, Shanghai 200240, China.

[4]School of Basic Medical Sciences, Shanghai Medical College Fudan University, Shanghai 200032, China

[5]Department of Pathology, Huashan hospital, Fudan University, Shanghai 200040, China

[#]These authors contributed equally.

*Correspondence:

haohankun@163.com (H.H.); feifeiluo@fudan.edu.cn (F.L.); ayayapple@hotmail.com (Y.W.)

Funding

This work was supported by the Shanghai ShenKang Hospital Development Centre (No. SHDC2020CR3038B and No. SHDC12024123)

Author contributions

H.H., F.L., Y.W., and M.M. initiated the study, formulated the scientific hypotheses, and outlined the experimental framework. M.M., Z.W., and J.H. executed the in vitro and in vivo assays, as well as evaluated the resulting data. K.F. and M.Y. performed the computational analysis on the bulk RNA-seq datasets. X.L., Y.Z., and X.Y. participated in maintaining the primary cell cultures. Jian W. and Zihao W. offered methodological advice for the vagotomy procedures. L.L., Q.Z., J.Z., W.L., W.C., Y.H., and X.S. contributed to the establishment of the tumor xenograft models. Y.W., H.H., F.L., and M.M. prepared the original draft of the article. Y.W., F.L., and H.H. oversaw the entire investigation and secured the necessary financial support. All authors critically evaluated and consented to the finalized manuscript.

Conflict of interest

The authors have declared that no competing interest exists.

ABSTRACT

Perineural invasion (PNI) is a well-recognized adverse prognostic indicator in gastric cancer (GC). However, the specific neural subsets infiltrating the tumor microenvironment and their mechanistic crosstalk with immune cells remain poorly characterized. To address this knowledge gap, we integrated clinicopathological analysis of a 365-patient GC cohort with TCGA-STAD data, and demonstrated that PNI independently predicted unfavorable outcomes and featured prominent cholinergic nerve infiltration; moreover, multiplex imaging visualized cholinergic nerve–B-cell–$CD8^+$ T-cell triads in the human GC stroma, offering direct evidence of local neuro-immune interplay. In vivo, nerve-derived acetylcholine (ACh) accelerated GC progression exclusively through immune-dependent routes, without directly stimulating tumor cell proliferation. Functionally, nerve-derived ACh elicited B cells to secrete immunosuppressive cytokines IL-10 and TGF-β, which subsequently compromised intratumoural $CD8^+$ T-cell cytotoxicity. Mechanistically, ACh triggered the MEK/ERK cascade in B cells, rewiring lipid metabolism and augmenting oxidative phosphorylation to bioenergetically support the secretion of these suppressive cytokines. Strikingly, MEK inhibition with trametinib completely abrogated the ACh-elicited B-cell metabolic adaptation, reinstated $CD8^+$ T-cell effector function, and potently inhibited GC outgrowth. Collectively, our findings uncover a cholinergic-driven neuro-immune-metabolic checkpoint in which neural signals exploit B-cell metabolic plasticity to orchestrate GC immune evasion, and we establish that targeting this B-cell-centric axis with MEK inhibitors offers a mechanistically grounded and clinically actionable strategy to reinvigorate antitumour immunity in gastric cancer.

INTRODUCTION

Gastric cancer (GC) remains a leading cause of cancer-related mortality worldwide, largely driven by its aggressive clinicopathological features[1–3]. Among these, perineural invasion (PNI)—the process by which neoplastic cells infiltrate and disseminate along nerve sheaths—is highly prevalent and clinically established as a robust, independent prognostic indicator of advanced disease and reduced survival[4–7]. However, while the prognostic utility of PNI is broadly recognized, the biological mechanisms underpinning nerve-driven tumor progression—specifically how innervating fibers interface with the multicellular tumor microenvironment (TME)—remain poorly defined.

Emerging paradigms in cancer neuroscience have fundamentally redefined the peripheral nervous system as an active instigator within the tumor-host ecosystem, rather than a passive structural bystander[8–11]. In solid tumors, infiltrating autonomic nerves release neurotransmitters that locally fuel malignant proliferation, tissue remodeling, and therapeutic resistance[12–14]. Densely innervated by the cholinergic fibers of the vagus nerve, the stomach serves as an archetypal model for elucidating these neuro-neoplastic interactions[13]. While prior studies indicate that vagal innervation and subsequent acetylcholine (ACh) release accelerate gastric tumorigenesis by stimulating early malignant transformation and expanding cancer stem cell populations[15], these investigations have predominantly focused on tumor-intrinsic responses, largely overlooking the broader impact of neural signaling on the multicellular TME.

Because adaptive immunity imposes the primary evolutionary constraint on malignant progression, the dense integration of cholinergic nerve fibers within the gastric TME implies an uncharacterized neural dimension of local immune regulation[13,16,17]. Whereas recent advances have begun to elucidate the immunomodulatory properties of sympathetic networks[18,19], the functional contribution of parasympathetic cholinergic circuits to the tumor immune landscape remains elusive. Crucially, the principles by which spatially restricted neurotransmitter gradients within the perineural niche govern the phenotypic

fates and dynamic interplay of infiltrating immune lineages constitute a major unresolved frontier in cancer neuroscience[20].

Here, by integrating clinical, spatial, and in vivo analyses, we elucidate how cholinergic innervation in PNI-positive GC drives progression by metabolically driving B cell-mediated immunosuppression. Mechanistically, ACh activates MEK/ERK signaling in tumor infiltrating B cells, triggering lipid-dependent OXPHOS rewiring. This licenses their secretion of IL-10 and TGF-β, directly impairing $CD8^+$ T cell cytotoxicity. Pharmacological MEK inhibition with trametinib disrupts this pathogenic circuit, reinstating anti-tumor immunity. Collectively, we decode a neuro-immune-metabolic relay, establishing the cholinergic–MEK–B cell axis as a targetable vulnerability against nerve-instructed tumor progression.

RESULTS

Perineural invasion is associated with poor prognosis and cholinergic nerve infiltration in human gastric cancer

To elucidate the clinical significance of PNI in GC, we evaluated a retrospective cohort of 365 patients following radical gastrectomy. Independent histopathological assessment by two blinded pathologists confirmed the presence of PNI in 51.5% (188/365) of tumors (Table 1; Fig. 1a), consistent with established prevalence rates[6,21]. PNI was significantly associated with aggressive disease hallmarks—including increased tumor size, advanced TNM stage, poor histological differentiation, and the presence of intravascular tumor emboli—while remaining independent of age, sex, histological subtype, and anatomical location.

To further validate the prognostic relevance of PNI across broader populations, we applied a previously established PNI-associated gene signature[22]. Using the TCGA-STAD dataset, we computed a quantitative PNI score for each tumor sample via gene set variation analysis (GSVA). Stratification of the cohort by the median PNI score revealed that patients in the PNI-high group had significantly worse overall survival (OS) and progression-free survival (PFS) (Fig. 1b). Moreover, PNI scores positively correlated with advanced tumor stages (Fig. 1c), supporting the clinical relevance of a PNI-associated transcriptional program in gastric adenocarcinoma progression.

To elucidate the molecular programs accompanying PNI-associated GC progression, we compared transcriptomic profiles between the PNI-high and PNI-low groups. Consistent with the neurotropic nature of PNI, gene sets related to nervous system development and axonogenesis were enriched in PNI-high tumors. Transcriptomic profiling indicated broad microenvironmental remodeling in PNI-high tumors, characterized by the enrichment of immune, TGF-β, and MAPK signaling pathways (Fig. 1d; Extended Data Fig. 1a). Within these global alterations, both KEGG and GO analyses convergently identified the enrichment of cholinergic synapse-related pathways. To further characterize this neural

signaling axis, we interrogated transcriptional programs associated with distinct autonomic nerve branches. Gene set enrichment analysis (GSEA) revealed significant enrichment of both cholinergic and adrenergic signaling pathways in PNI-high tumors (Fig. 1e). To determine which autonomic branch functionally predominates *in situ*, we quantified norepinephrine (NE) and ACh levels in fresh GC tissues via enzyme-linked immunosorbent assay (ELISA). ACh concentrations were significantly elevated in PNI-positive tissues compared with PNI-negative counterparts, whereas NE levels remained unchanged (Fig. 1f). Subsequent multiplex immunofluorescence (mIF) profiling of GC tissues revealed robust neural infiltration in PNI-positive patients (Fig. 1g) and 24.5% of $PGP9.5^+$ nerve fibers co-expressed choline acetyltransferase (ChAT), compared with only 8.1% that expressed tyrosine hydroxylase (TH) (Fig. 1h–i).

Collectively, these data indicate that PNI drives a clinically aggressive phenotype in GC, characterized by prominent cholinergic innervation and enhanced local ACh level.

Cholinergic signaling promotes immune-dependent tumor growth in gastric cancer

To investigate the role of cholinergic signaling in GC progression, we established an orthotopic GC model in immunocompetent 615 mice. Subdiaphragmatic vagotomy was performed in 7-week-old mice (Extended Data Fig. 2a), which significantly reduced local gastric ACh levels compared with sham-operated controls, as confirmed by ELISA (Extended Data Fig. 2b). Following orthotopic murine forestomach carcinoma (MFC) cell implantation (Fig. 2a), vagotomy significantly reduced tumor burden, decreasing the tumor area fraction by 44% compared with sham-operated controls (Fig. 2b–c; Extended Data Fig. 2c). In contrast, when the same surgical intervention was performed in immunodeficient NSG mice (lacking mature T, B, and NK cells), the tumor-suppressive effect of vagotomy was largely abrogated (Fig. 2d–f; Extended Data Fig. 2d). Notably, although the tumor area fraction was comparable between the 615 and NSG orthotopic models—likely attributable to the larger baseline stomach size of NSG mice—the marked

difference in absolute tumor area underscores the critical role of an intact immune system in mediating vagus nerve-driven tumor progression.

Given that ACh serves as the principal neurotransmitter of the vagus nerve[23], we subsequently established an identical orthotopic GC model in immunocompetent 615 mice to assess the impact of exogenous ACh administration (Fig. 2g). Consistent with the vagotomy results, ACh supplementation potentiated tumor progression, resulting in a 65% increase in the tumor area fraction relative to PBS-treated controls (Fig. 2h–i; Extended Data Fig. 2e). These findings were faithfully recapitulated in a subcutaneous MFC model in 615 mice (Fig. 2j), where daily ACh treatments significantly accelerated tumor progression, evidenced by a 59% increase in both tumor weight and volume (Fig. 2k–m), without affecting gross body weight (Extended Data Fig. 2f). Conversely, in immunodeficient NSG mice, exogenous ACh failed to exert any tumor-promoting effects and did not affect overall body weight (Fig. 2n–q; Extended Data Fig. 2g), indicating that the tumor-promoting effect of ACh is immune-dependent. To exclude direct, tumor-intrinsic oncogenic effects of ACh, we evaluated its impact on GC cell lines (MFC and HGC-27) *in vitro*. Apoptosis assays showed that ACh treatment did not significantly alter apoptotic rates in GC cells (Fig. 2r; Extended Data Fig. 2h). Transwell assays further revealed that ACh did not enhance the migratory capacity of HGC-27 cells; rather, it exerted a slight inhibitory effect on MFC cell migration (Fig. 2s; Extended Data Fig. 2i). Moreover, cell cycle progression (Fig. 2t; Extended Data Fig. 2j) and temporal proliferation dynamics (via CCK-8) remained unaffected by ACh exposure (Fig. 2u; Extended Data Fig. 2k).

Collectively, these complementary *in vivo* and *in vitro* observations underscore that an intact immune system is indispensable for the tumor-promoting effects of cholinergic signaling and its principal neurotransmitter ACh.

Cholinergic signaling induces immunosuppressive phenotypes of B cells and functional impairment of $CD8^+$ T cells within the tumor microenvironment

To elucidate how local cholinergic signaling modulates GC progression through immune-dependent mechanisms, we characterized the immune landscape using flow cytometry (gating strategy in Extended Data Fig. 3a–b). After vagotomy, the overall frequencies of major immune subsets remained largely unperturbed in both the peripheral circulation (Extended Data Fig. 4a) and the TME (Extended Data Fig. 4b). However, phenotypic analysis revealed that tumor-infiltrating B cells from vagotomized mice exhibited decreased expression of regulatory B cell (Breg)-associated markers (Tim-1, CD38, and CD1d) and immunosuppressive cytokines (IL-10 and TGF-β)[24–27] (Fig. 3a). Concomitantly, intratumoral $CD8^+$ T cells shifted toward an enhanced anti-tumor effector profile, evidenced by the upregulation of perforin and IFN-γ (Fig. 3a). Conversely, exogenous ACh administration in both orthotopic (Fig. 3b; Extended Data Fig. 4c) and subcutaneous (Fig. 3c; Extended Data Fig. 4d) GC models reversed these dynamics, enriching the immunosuppressive phenotypes of B cells while attenuating the expression of effector molecules in $CD8^+$ T cells—without altering the overall proportions of major immune subsets within the TME.

Given that both B cells and $CD8^+$ T cells underwent significant phenotypic shifts, we next examined their spatial relationships with tumor-innervating nerves in human GC tissues. mIF revealed a preferential enrichment of both B cells and $CD8^+$ T cells within perineural niches compared with nerve-distal regions, whereas $CD4^+$ T cells were mostly absent from these microdomains (Fig. 3d). Prompted by this co-localization within the perineural niche, we interrogated denervation-induced transcriptomic shifts using an independent dataset (GSE30295). Notably, B cell activation signatures were among the most prominently downregulated pathways following vagotomy in murine orthotopic GC (Fig. 3e). Thus, to specifically delineate the spatial distribution of nerve–B cell proximity and capture the entire B cell lineage—accounting for CD19 downregulation in terminally differentiated plasma cells[28]—we utilized a CD19/CD138 dual-staining approach in human GC tissues. This revealed a marked accumulation of B-lineage cells in the immediate vicinity of PNI-positive nerves (Fig. 3f). Furthermore, morphometric quantification indicated

that nerve–B cell distances predominantly fell within a 10–80 μm radius (Fig. 3g–h), a spatial distribution consistent with paracrine signaling mediated by neurotransmitter and cytokine diffusion rather than direct synaptic contact[29].

Collectively, these findings indicate that local cholinergic signaling shapes an immunosuppressive microenvironment characterized by the induction of immunosuppressive phenotypes in B cells and the concomitant functional attenuation of intratumoral $CD8^+$ T cells.

ACh induces an IL-10/TGF-β secretory axis in B cells to suppress $CD8^+$ T cells

To delineate how cholinergic signaling specifically modulates T and B cell functions, we first exposed purified murine splenic $CD8^+$ T cells directly to an ACh concentration gradient, which was designed to reflect the fact that while steady-state neurotransmitter levels in the tumor microenvironment are typically nanomolar to low micromolar, localized concentrations within the perineural niche can reach up to 200 μM[30]. Notably, exposing $CD8^+$ T cells to ACh within this physiological range did not significantly alter perforin or IFN-γ expression. Direct suppression of $CD8^+$ T cell effector function—without compromising cell viability (Fig. 4a)—was observed only at a supraphysiological concentration of 400 μM (Fig. 4b), implying that *in vivo* cholinergic suppression of $CD8^+$ T cells likely requires a cellular intermediary rather than occurring via direct action.

To test whether B cells serve as this intermediary, we evaluated primary murine splenic B cells activated *in vitro* via T cell-dependent (TD) or T cell-independent (TI) pathways[31–33]. ACh exposure (50 μM) skewed B cells toward an immunosuppressive phenotype. Flow cytometric analysis revealed a >50% increase in IL-10 and TGF-β protein levels under both TI (Fig. 4c) and TD (Fig. 4d) conditions, which was corroborated at the transcriptional level by qRT-PCR for *Il10* and *Tgfb1* (Fig. 4e). Concomitantly, ACh attenuated the expression of the pro-inflammatory cytokine TNF-α and robustly upregulated canonical Breg-associated

surface markers, including Tim-1, CD38, and CD1d, in TI-activated B cells (Fig. 4f).

To determine whether ACh-educated B cells mediate $CD8^+$ T cell dysfunction, we employed an *in vitro* indirect co-culture system (Fig. 4g). $CD8^+$ T cells co-cultured with ACh-pretreated B cells exhibited a significant reduction in perforin and IFN-γ production relative to those co-cultured with PBS-pretreated B cells; importantly, direct exposure of $CD8^+$ T cells to ACh (50 μM) failed to induce this suppression (Fig. 4h), confirming that the impairment is strictly B cell-mediated. Furthermore, exogenous treatment with recombinant IL-10 or TGF-β, either alone or in combination, recapitulated this T cell effector suppression (Fig. 4i). Conversely, neutralizing IL-10 and TGF-β in the co-culture system largely abrogated the suppressive capacity of ACh-educated B cells (Fig. 4j), identifying these cytokines as key functional mediators of this cross-talk.

Finally, we performed an *in vivo* B cell depletion assay using an anti-CD19 neutralizing antibody in a syngeneic 615 GC model (Fig. 4k). Targeted B cell depletion resulted in a ~60% reduction in both tumor weight and volume, effectively abrogating the pro-tumorigenic effects of exogenous ACh administration (Fig. 4l–n). Furthermore, following successful B cell depletion (Fig. 4o), the expression of cytotoxic effector molecules (perforin, IFN-γ, and GzmB) in tumor-infiltrating $CD8^+$ T cells increased by ~160%, ~220%, and ~150%, respectively, compared to the ACh-treated isotype controls (Fig. 4p), indicating that ACh-mediated functional impairment of $CD8^+$ T cells is largely B cell-dependent.

To corroborate these mechanistic insights within a clinical context, we stratified patients from the TCGA-STAD cohort into PNI-high and PNI-low groups based on the established PNI signature. GSEA revealed a significant enrichment of the B cell receptor signaling pathway within the PNI-high cohort (Fig. 4q). Spatial colocalization of B cells with IL-10 and TGF-β was also primarily observed in the vicinity of PNI regions, as shown by mIF staining of human GC histological sections (Fig. 4r).

Collectively, these findings demonstrate that ACh promotes B cells to produce IL-10 and TGF-β, thereby suppressing $CD8^+$ T cell function.

ACh promotes IL-10/TGF-β production of B cells through a MEK/ERK-driven lipid-OXPHOS metabolic axis

To elucidate the mechanisms underlying ACh-mediated B cell regulation, we first investigated the cognate receptors involved. Consistent with previous reports[34,35], our RNA sequencing data confirmed that B cells concurrently express multiple subtypes of both muscarinic (mAChR) and nicotinic (nAChR) acetylcholine receptors (Extended Data Fig. 5a). Accordingly, activated B cells were treated with ACh in the presence of the mAChR-specific antagonist atropine or the nAChR-specific antagonist mecamylamine. Pharmacological blockade of either receptor significantly attenuated the ACh-driven upregulation of IL-10 and TGF-β (Extended Data Fig. 5b–c), indicating that ACh regulates B cell function via coordinated muscarinic and nicotinic signaling.

Next, targeted transcript analysis revealed that ACh treatment did not significantly alter the expression of master transcription factors governing B cell maturation and germinal center dynamics, including *Pax5*, *Prdm1*, *Xbp1*, *Bach2*, and *Bcl6*[36–40] (Extended Data Fig. 5d). Consistent with this transcriptional stability, flow cytometry confirmed that ACh exposure neither substantially altered B cell differentiation nor impaired antibody production (Extended Data Fig. 5e). Next, the transcriptomes of ACh-stimulated B cells were analyzed by GO (Fig. 5a) and GSEA (Fig. 5b). ACh-regulated gene networks were highly enriched for the ERK signaling cascade, lipid metabolic processing, and B cell-mediated immunity (Fig. 5a–b). Furthermore, intersection analysis revealed that differentially expressed genes shared between ERK signaling and lipid metabolism pathways were consistently upregulated following ACh treatment (Extended Data Fig. 5f). Western blot analysis validated that ACh stimulation elicited rapid and robust phosphorylation of MEK and ERK (peaking at 10–20 minutes), while leaving the p38 MAPK pathway unaffected under both TD- and TI-activation conditions (Fig. 5c; Extended Data Fig. 5g). Crucially, targeted inhibition of either MEK (trametinib) or ERK (SCH772984)

suppressed ACh-induced cytokine production, reducing IL-10 and TGF-β levels by ~80% and ~50%, respectively (Fig. 5d).

To investigate whether ACh signaling drives specific metabolic adaptations in B cells via the MEK/ERK pathway, we used fluorescent fatty acid analogs (BODIPY 500/510 and BODIPY 493/503) and observed that ACh stimulation significantly increased both fatty acid uptake and intracellular lipid accumulation (Fig. 5e). These effects were largely reversed by pharmacological inhibition of either MEK (trametinib) or ERK (SCH772984) (Fig 5e; Extended Data Fig. 5h). In contrast, ACh did not alter glucose uptake, as assessed by 2-NBDG staining (Fig. 5f). Given that intracellular lipids frequently serve as substrates for OXPHOS through fatty acid oxidation (FAO)[41], we next evaluated B cell mitochondrial bioenergetics. Real-time metabolic flux analysis revealed that compared with vehicle controls, ACh augmented OXPHOS, as evidenced by concurrent increases in basal and maximal respiration, ATP production, and spare respiratory capacity (Fig. 5g–h). Pharmacological blockade with the CPT1a inhibitor etomoxir or the MEK inhibitor trametinib attenuated the ACh-induced respiratory enhancement by ~40% and ~70%, respectively (Fig. 5g–h).

Notably, the ACh-induced expression of both IL-10 and TGF-β was reduced by ~35% following lipid metabolism blockade (etomoxir) and by ~65% upon OXPHOS inhibition (rotenone/oligomycin). In contrast, blockade of glycolysis (2-DG) or glutaminolysis (BPTES) showed no such effects (Fig. 5i–j). Of note, ACh-induced ERK phosphorylation remained largely unaffected despite metabolic blockade with etomoxir or oligomycin (Fig. 5k).

Collectively, these findings delineate a mechanistic pathway in which ACh activates the MEK/ERK cascade, which subsequently promotes lipid–OXPHOS metabolic reprogramming to enable B cell secretion of suppressive cytokines.

Trametinib attenuates immunosuppressive B cell activity and enhances CD8$^+$ T cell-

mediated anti-tumor immunity in gastric cancer

To evaluate the translational potential of targeting the MEK/ERK axis to alleviate ACh-mediated B cell immunosuppression, we established subcutaneous MFC tumors in immunocompetent 615 mice and treated them with daily ACh, either alone or in combination with oral trametinib (Fig. 6a). Exogenous ACh administration significantly accelerated tumor growth; in contrast, trametinib treatment substantially suppressed tumor progression and effectively abrogated the pro-tumorigenic effects of ACh (Fig. 6b), as evidenced by a ~70% reduction in both tumor volume and weight relative to the ACh-treated group (Fig. 6c–d). Immunohistochemical analysis of tumor sections revealed that whereas ACh alone had no significant impact on Ki-67 or cleaved caspase-3 expression, trametinib treatment induced a trend toward reduced tumor proliferation (Ki-67) concomitant with a significant increase in tumor cell apoptosis (cleaved caspase-3) (Fig. 6e–f), which was further validated by in vitro experiments demonstrating the direct inhibitory effect of trametinib on tumor growth (Extended Data Fig. 6a–d). Furthermore, immune profiling of the TME demonstrated that exogenous ACh increased IL-10 and TGF-β expression in tumor-infiltrating B cells, an effect that was largely reversed by trametinib (Fig. 6g). This trametinib-mediated blockade of B cell suppressive function was accompanied by the restoration of effector molecule expression (e.g., IFN-γ, and GzmB) in intratumoral $CD8^+$ T cells (Fig. 6h).

Collectively, these in vivo findings suggest that trametinib not only restricts intrinsic tumor viability but also effectively remodels the immune landscape by suppressing B cell-derived immunosuppressive cytokines, thereby reinvigorating $CD8^+$ T cell-mediated anti-tumor immunity.

DISCUSSION

While PNI is clinically established as a critical determinant of poor prognosis in GC[6], the specific neural subtypes driving this process and their functional interactions within the TME remain fundamentally unresolved. Here, we delineate a previously unrecognized neuro-immune-metabolic axis in GC, characterized by dense cholinergic innervation. Rather than exerting direct oncogenic effects on malignant cells, nerve-derived ACh actively sculpts an immunosuppressive niche. Specifically, ACh programs infiltrating B cells into a tolerogenic state through MEK/ERK-dependent rewiring of lipid metabolism and OXPHOS. These neurally educated B cells subsequently abrogate $CD8^+$ T cell-mediated cytotoxicity. Consequently, pharmacological disruption of this neuro-immune circuitry via MEK inhibition fundamentally remodels the tumor immune landscape, providing a compelling mechanistic rationale for precision immunotherapeutic interventions in GC.

The dynamic interplay between malignant lesions and the peripheral nervous system serves as a fundamental driver of disease progression[13]. Solid tumors actively secrete neurotrophic signals to promote intra-tumoral innervation, an event that not only precipitates debilitating neuropathic pain but also allows cancer cells to co-opt neural circuitry—particularly vagal networks—to facilitate their own proliferation and dissemination[12]. Although murine models have implied that vagotomy curtails GC progression[14,15], clinical vagotomy during radical gastrectomy currently lacks defined oncological indications, typically occurring merely as a passive anatomical consequence of achieving R0 resection[42]. Paralleling these observations, our in vivo data demonstrate that denervation substantially restricts tumor growth and abrogates the accumulation of immunosuppressive cytokines in orthotopic GC models suggesting that intentional vagal denervation could be evaluated as a targeted therapeutic intervention for GC patients harboring severe PNI. Cholinergic signaling, primarily orchestrated by ACh and its cognate receptors (AChRs), serves as the critical conduit bridging vagal innervation and the TME, driving both angiogenesis and immune evasion[43]. Although recent study reported the role of ACh–AChR axis in the regulation of the innate immune responses (e.g., ILC3s) to neural

signals[14], its regulation of the adaptive immunity and the associated intracellular metabolic rewiring remain poorly understood. Our spatial and mechanistic analyses reveal a broader systemic impact: vagal-derived ACh dictates the phenotypic fate of the adaptive immune repertoire (e.g., B cells and $CD8^+$ T cells), providing a critical mechanistic link to overcome the limitations of current T cell-centric immunotherapies.

A central paradigm-shifting aspect of our findings is the identification of B cells as the primary cellular intermediaries in nerve-driven immunosuppression. The role of B cells in solid tumors has historically been controversial, with conflicting reports describing both anti-tumorigenic and pro-tumorigenic functions[44–47]. Our spatial morphometric analysis resolves this paradox by demonstrating that the tolerogenic phenotype of B cells is highly anatomically restricted. We found that B cells preferentially accumulate within a 10–80 μm radius of cholinergic fibers, a spatial configuration perfectly suited for paracrine neurotransmitter gradients. By exposing B cells to physiological concentrations of ACh, we demonstrated that cholinergic signaling dominantly polarizes them toward an IL-10/TGF-β-secreting phenotype, which is essential for the subsequent functional exhaustion of local $CD8^+$ T cells[48]. This spatial neuro-immune relay elegantly explains why high cholinergic innervation correlates with robust immune evasion, highlighting that immune cell functional plasticity is heavily dictated by their proximity to the perineural niche.

Mechanistically, we uncover a novel intersection between neurotransmitter signaling and immunometabolism. The activation of B cells and their subsequent cytokine production are intrinsically linked to their metabolic fitness[32,49,50]. We reveal that ACh-induced mAChR/nAChR signaling converges on the MEK/ERK cascade, which subsequently drives a profound lipid-OXPHOS metabolic adaptation. Unlike conventional B cell activation that heavily relies on glycolysis[51], this ACh-instructed lipid uptake and enhanced mitochondrial respiration specifically license B cells to sustain the energetic demands of immunosuppressive cytokine secretion. The uncoupling of this metabolic dependency via OXPHOS or lipid metabolism inhibitors efficiently reversed the tolerogenic phenotype. This finding expands the classical understanding of neurotransmitters from mere

electrophysiological or survival signals to potent metabolic modulators within the TME, representing a major conceptual advance in cancer neuroscience.

Translating these biological insights into therapeutic vulnerabilities, we evaluated the repurposing of trametinib, an FDA-approved MEK inhibitor traditionally utilized for BRAF/MEK-mutant solid tumors[52]. While kinase inhibitors are typically deployed for their direct cytostatic effects on tumor cells, our data highlight a potent, off-target immunomodulatory benefit. Systemic trametinib administration effectively uncoupled the cholinergic–MEK–B cell axis, extinguishing B cell-derived IL-10 and TGF-β production and reinvigorating $CD8^+$ T cell cytotoxicity. This dual mechanism of action—simultaneously suppressing tumor intrinsic viability and dismantling nerve-driven immune tolerance—positions MEK inhibition as a highly promising strategy to overcome immune resistance in heavily innervated, PNI-positive gastric cancers.

In conclusion, our study decodes a critical neuro-immune-metabolic circuitry underlying GC progression. By defining how cholinergic nerves hijack B cell metabolism to enforce localized immune privilege, we establish a new framework for understanding PNI. Targeting this neural signaling cascade, either through metabolic blockade or repurposed MEK inhibitors, offers a rational therapeutic avenue to dismantle the neuro-neoplastic ecosystem and restore anti-tumor immunity in advanced gastric cancer.

REFERENCE

1. Patel, A. K., Sethi, N. S. & Park, H. Gastric cancer: A review. *JAMA* **335**, 439–450 (2026).

2. Sundar, R. *et al.* Gastric cancer. *Lancet Lond. Engl.* **405**, 2087–2102 (2025).

3. Lin, Y., Zheng, Y., Wang, H.-L. & Wu, J. Global patterns and trends in gastric cancer incidence rates (1988-2012) and predictions to 2030. *Gastroenterology* **161**, 116-127.e8 (2021).

4. Liebig, C., Ayala, G., Wilks, J. A., Berger, D. H. & Albo, D. Perineural invasion in cancer: a review of the literature. *Cancer* **115**, 3379–3391 (2009).

5. Zhao, B. *et al.* Perineural invasion as a predictive factor for survival outcome in gastric cancer patients: a systematic review and meta-analysis. *J. Clin. Pathol.* **73**, 544–551 (2020).

6. Deng, J. *et al.* Prognostic value of perineural invasion in gastric cancer: a systematic review and meta-analysis. *PloS One* **9**, e88907 (2014).

7. Li, Y. *et al.* Long noncoding RNA DIAPH2-AS1 promotes neural invasion of gastric cancer via stabilizing NSUN2 to enhance the m5C modification of NTN1. *Cell Death Dis.* **14**, 260 (2023).

8. Monje, M. *et al.* Roadmap for the emerging field of cancer neuroscience. *Cell* **181**, 219–222 (2020).

9. Zahalka, A. H. & Frenette, P. S. Nerves in cancer. *Nat. Rev. Cancer* **20**, 143–157 (2020).

10. Winkler, F. *et al.* Cancer neuroscience: State of the field, emerging directions. *Cell* **186**, 1689–1707 (2023).

11. Zhang, Y. *et al.* Neuroimmunometabolic co-evolution in the tumor micro- and macroenvironment. *Cell Metab.* **38**, S1550-4131(26)00044–6 (2026).

12. Amit, M., Na'ara, S. & Gil, Z. Mechanisms of cancer dissemination along nerves. *Nat. Rev. Cancer* **16**, 399–408 (2016).

13. Vaes, N., Idris, M., Boesmans, W., Alves, M. M. & Melotte, V. Nerves in gastrointestinal cancer: from mechanism to modulations. *Nat. Rev. Gastroenterol. Hepatol.* **19**, 768–784 (2022).

14. Liao, F. *et al.* Nerves stimulates crosstalk between gastric cancer and group 3 innate lymphoid cells to enhance immunosuppression. *Cancer Res.* **86**, 1968–1986 (2026).

15. Zhao, C.-M. *et al.* Denervation suppresses gastric tumorigenesis. *Sci. Transl. Med.* **6**, 250ra115 (2014).

16. Zeng, D. *et al.* Tumor microenvironment characterization in gastric cancer identifies prognostic and immunotherapeutically relevant gene signatures. *Cancer Immunol. Res.* **7**, 737–750 (2019).

17. Yasuda, T. & Wang, Y. A. Gastric cancer immunosuppressive microenvironment heterogeneity: implications for therapy development. *Trends Cancer* **10**, 627–642 (2024).

18. Liu, T. *et al.* A local sympathetic-immune axis inhibits melanoma growth in mice by dictating adrenergic control. *Neuron* **114**, 1576-1593.e8 (2026).

19. Fnu, T. *et al.* Sympathetic neurons promote small cell lung cancer through the β2-adrenergic receptor. *Cancer Discov.* **15**, 616–632 (2025).

20. Teratani, T., Mikami, Y. & Kanai, T. Neuroimmune crosstalk in the gut and liver. *Int. Immunol.* **34**, 475–484 (2022).

21. Bilici, A. *et al.* Prognostic significance of perineural invasion in patients with gastric cancer who underwent curative resection. *Ann. Surg. Oncol.* **17**, 2037–2044 (2010).

22. Warren, T. A. *et al.* Expression profiling of cutaneous squamous cell carcinoma with perineural invasion implicates the p53 pathway in the process. *Sci. Rep.* **6**, 34081 (2016).

23. Borovikova, L. V. *et al.* Vagus nerve stimulation attenuates the systemic inflammatory response to endotoxin. *Nature* **405**, 458–462 (2000).

24. Zhu, H. *et al.* Intratumoral CD38+CD19+B cells associate with poor clinical outcomes and immunosuppression in patients with pancreatic ductal adenocarcinoma. *EBioMedicine* **103**, 105098 (2024).

25. Bod, L. *et al.* B-cell-specific checkpoint molecules that regulate anti-tumour immunity. *Nature* **619**, 348–356 (2023).

26. Ding, Q. *et al.* Regulatory B cells are identified by expression of TIM-1 and can be induced through TIM-1 ligation to promote tolerance in mice. *J. Clin. Invest.* **121**, 3645–3656 (2011).

27. Yanaba, K. *et al.* A regulatory B cell subset with a unique CD1dhiCD5+ phenotype controls T cell-dependent inflammatory responses. *Immunity* **28**, 639–650 (2008).

28. Ahmad, S. B. & Jefferson, J. A. Targeting B cells and plasma cells in glomerular disease. *J. Am. Soc. Nephrol. JASN* **36**, 1844–1857 (2025).

29. Liu, Y. *et al.* Conserved spatial subtypes and cellular neighborhoods of cancer-

associated fibroblasts revealed by single-cell spatial multi-omics. *Cancer Cell* **43**, 905-924.e6 (2025).

30. Clements, J. D. Transmitter timecourse in the synaptic cleft: its role in central synaptic function. *Trends Neurosci.* **19**, 163–171 (1996).

31. Zhang, B. *et al.* B cell-derived GABA elicits IL-10+ macrophages to limit anti-tumour immunity. *Nature* **599**, 471–476 (2021).

32. Bradford, H. F. *et al.* Thioredoxin is a metabolic rheostat controlling regulatory B cells. *Nat. Immunol.* **25**, 873–885 (2024).

33. Wang, Z. *et al.* Leucine-tRNA-synthase-2-expressing B cells contribute to colorectal cancer immunoevasion. *Immunity* **55**, 1067-1081.e8 (2022).

34. Kurata-Sato, I. *et al.* Vagus nerve stimulation modulates distinct acetylcholine receptors on B cells and limits the germinal center response. *Sci. Adv.* **10**, eadn3760 (2024).

35. Zeng, Q. *et al.* Spleen fibroblastic reticular cell-derived acetylcholine promotes lipid metabolism to drive autoreactive B cell responses. *Cell Metab.* **35**, 837-854.e8 (2023).

36. Cobaleda, C., Schebesta, A., Delogu, A. & Busslinger, M. Pax5: the guardian of B cell identity and function. *Nat. Immunol.* **8**, 463–470 (2007).

37. Shaffer, A. L. *et al.* Blimp-1 orchestrates plasma cell differentiation by extinguishing the mature B cell gene expression program. *Immunity* **17**, 51–62 (2002).

38. Reimold, A. M. *et al.* Plasma cell differentiation requires the transcription factor XBP-1. *Nature* **412**, 300–307 (2001).

39. Muto, A. *et al.* The transcriptional programme of antibody class switching involves the repressor BacH2. *Nature* **429**, 566–571 (2004).

40. Tunyaplin, C. *et al.* Direct repression of prdm1 by bcl-6 inhibits plasmacytic differentiation. *J. Immunol. Baltim. Md 1950* **173**, 1158–1165 (2004).

41. Rambold, A. S., Cohen, S. & Lippincott-Schwartz, J. Fatty acid trafficking in starved cells: regulation by lipid droplet lipolysis, autophagy, and mitochondrial fusion dynamics. *Dev. Cell* **32**, 678–692 (2015).

42. Sun, K.-K., Shen, X.-J., Hua, P., Zhang, Y.-F. & Wu, Y.-Y. Vagus nerve preservation and double-flap technique in laparoscopic proximal gastrectomy. *Front. Surg.* **12**, 1656058 (2025).

43. Sampaio Moura, N. *et al.* Cholinergic mechanisms in gastrointestinal neoplasia. *Int.*

J. Mol. Sci. **25**, 5316 (2024).

44. Rosser, E. C. & Mauri, C. Regulatory B cells: origin, phenotype, and function. *Immunity* **42**, 607–612 (2015).

45. Li, Z. *et al.* B-cell performance in chemotherapy: Unravelling the mystery of B-cell therapeutic potential. *Clin. Transl. Med.* **14**, e1761 (2024).

46. Zhang, E. *et al.* Roles and mechanisms of tumour-infiltrating B cells in human cancer: a new force in immunotherapy. *Biomark. Res.* **11**, 28 (2023).

47. Laumont, C. M. & Nelson, B. H. B cells in the tumor microenvironment: Multi-faceted organizers, regulators, and effectors of anti-tumor immunity. *Cancer Cell* **41**, 466–489 (2023).

48. Mirlekar, B. Tumor promoting roles of IL-10, TGF-β, IL-4, and IL-35: its implications in cancer immunotherapy. *SAGE OPEN Med.* **10**, 20503121211069012 (2022).

49. Li, R. *et al.* Oxidative phosphorylation regulates B cell effector cytokines and promotes inflammation in multiple sclerosis. *Sci. Immunol.* **9**, eadk0865 (2024).

50. Martinis, E. *et al.* B cell immunometabolism in health and disease. *Nat. Immunol.* **26**, 366–377 (2025).

51. Caro-Maldonado, A. *et al.* Metabolic reprogramming is required for antibody production that is suppressed in anergic but exaggerated in chronically BAFF-exposed B cells. *J. Immunol.* **192**, 3626–3636 (2014).

52. Flaherty, K. T. *et al.* Improved survival with MEK inhibition in BRAF-mutated melanoma. *N. Engl. J. Med.* **367**, 107–114 (2012).

METHODS

Clinical specimen collection

Tissue samples were collected from patients with GC who underwent radical gastrectomy at Huashan Hospital affiliated to Fudan University. Informed consent was obtained from all subjects involved and the project was approved by the Ethical Committee of Medical Research, Huashan Hospital of Fudan University (No. KY2026-1023).

Patient and public involvement

Neither patients nor the public were involved in the conceptualization, design, recruitment, or execution of this study. The research framework did not incorporate patient priorities, experiences, or preferences, and individual findings will not be disseminated to the participants.

Cell lines and cell culture

The HGC-27 and MFC cell lines were obtained from Shanghai Fuheng Biology (China). All cell lines were authenticated by short tandem repeat (STR) profiling and routinely tested to ensure they were mycoplasma-free. Both cell lines were cultured in RPMI-1640 medium (Gibco, USA) supplemented with 10% fetal bovine serum (FBS, Gibco, USA) and 1% penicillin/streptomycin (Beyotime, China) in a humidified incubator with 5% CO_2 at 37°C.

In vitro B cells isolation and activation

Bulk B cells were isolated from murine splenocytes utilizing a B cell isolation kit (STEMCELL, Canada) following the manufacturer's instructions. Purified B cells (>95%

purity) were cultured in RPMI-1640 medium supplemented with 10% FBS at a density of 1 × 10^6 cells/mL. For in vitro activation, naive B cells were stimulated using one of two distinct paradigms: (1) lipopolysaccharide (LPS, 10 μg/mL, Sigma-Aldrich, USA) combined with β-mercaptoethanol (β-ME, 50 μM, Sigma-Aldrich); or (2) anti-IgM (10 μg/mL, Thermo Fisher, USA), anti-CD40 (10 μg/mL, Thermo Fisher), and β-ME (50 μM, Sigma-Aldrich). Cells were cultured at 37°C with 5% CO_2 for the indicated durations prior to further analysis.

Mouse experiments

For *in vivo* tumor modeling, 6- to 8-week-old 615 and NSG mice were purchased from Shanghai Chengxi Biotech (China) and all animal procedures were approved by the Institutional Animal Care and Use Committee (IACUC Issue No. CX052604158). To establish the orthotopic GC model, mice were randomly assigned to either a bilateral subdiaphragmatic vagotomy cohort or a sham-operated control cohort. Following anesthesia with 2% sodium pentobarbital, a 1-cm laparotomy was performed. Under a surgical stereomicroscope, the vagal trunks innervating the abdominal esophagus and stomach were identified and completely transected. In sham-operated mice, the vagal nerves were exposed but left intact. Following a 7-day recovery period, MFC cells (4 × 10^5 cells in 40 μL of PBS) were injected into the gastric subserosa using a 50-μL Hamilton syringe (USA). For the subcutaneous model, mice were inoculated with 3 × 10^5 MFC cells into the left flank or bilaterally. Upon reaching a palpable tumor volume of 50–100 mm^3, mice were randomized into treatment cohorts to ensure equivalent baseline tumor burdens. Tumor dimensions and body weights were monitored every 2–3 days. Tumor volumes were calculated as $V = (Length \times Width^2)/2$. Humane endpoints were strictly enforced; mice were euthanized if tumor volume exceeded 2,000 mm^3, severe ulceration occurred, or weight loss exceeded 20%.

Tissue preparation

Peripheral blood, collected via cardiac puncture, was dispensed into tubes containing 20 μL of 0.5 M EDTA (Thermo Fisher). Erythrocytes were depleted using ACK lysis buffer (Thermo Fisher) for 4 min, quenched with 1% FBS-supplemented PBS, and centrifuged at 400 g for 5 min. A secondary 3-min lysis step was performed if necessary to ensure high purity. Solid tumors were mechanically minced and enzymatically dissociated using Mouse/Human Tumor Dissociation Kits in gentleMACS C tubes (Miltenyi Biotec, Germany) following the manufacturer's protocols. Suspensions were filtered through 70-μm sterile strainers, treated with ACK lysis buffer, and re-filtered to yield single-cell suspensions.

Transwell migration assay

Cell migration assays were performed using 24-well Transwell inserts (8.0 μm pore size; Corning, USA). HGC-27 and MFC cells (1×10^5) suspended in 200 μL of serum-free medium were seeded into the upper chambers. The lower chambers were filled with 500 μL of medium supplemented with 10% FBS as a chemoattractant. Following a 20-h incubation at 37°C, non-migratory cells on the apical surface of the membrane were mechanically removed using cotton swabs. Migrated cells on the basal surface were fixed with 4% paraformaldehyde, stained with 0.1% crystal violet, and imaged using bright-field microscopy. For quantification, cells in five randomly selected fields per insert were counted using ImageJ software (v1.54s).

Cell cycle and apoptosis test

For cell cycle profiling, cells were fixed in ice-cold 70% ethanol overnight at -20°C. Following fixation, cells were washed and incubated with RNase A and propidium iodide (PI, Thermo Fisher) to stain total DNA content. Cell cycle distribution was subsequently

acquired using flow cytometry. To evaluate apoptosis, both adherent and floating cells were harvested, washed, and resuspended in Annexin V binding buffer (Biolegend, USA). The cell suspensions were co-stained with Annexin V-FITC (Biolegend) and 7-aminoactinomycin D (7-AAD, Thermo Fisher) for 15 min at room temperature in the dark. Apoptotic fractions were analyzed via flow cytometry within 1 h of staining. All flow cytometric data were analyzed using FlowJo software (v10.8.1).

Immunofluorescence staining

Formalin-fixed, paraffin-embedded (FFPE) tissue sections were deparaffinized and rehydrated. Heat-induced epitope retrieval was performed in sodium citrate buffer (pH 6.0) for 15 min. Sections were blocked with 5% bovine serum albumin (BSA) for 30 min at 37°C and incubated overnight at 4°C with specific primary antibodies. Following PBS washes, sections were incubated with fluorophore-conjugated secondary antibodies for 1 h at 37°C. Nuclei were counterstained with DAPI. Slides were mounted with anti-fade medium. Fluorescent images were acquired using a scanner and visualized using CaseViewer software (v2.4).

Tumor cell proliferation assay

Cellular proliferation of the MFC and HGC-27 cell lines was assessed using the Cell Counting Kit-8 (CCK-8) assay (Beyotime). Cells were seeded into 96-well plates at a density of 2×10^3 cells per well and allowed to adhere overnight. The cells were subsequently treated with ACh (50 μM, Sigma-Aldrich) or a vehicle control. Viability was assessed every 24 h over 5 days. Following a 1-h incubation with CCK-8 reagent at 37°C, absorbance was measured at 450 nm using a microplate reader. Cell proliferation rate was calculated by comparing the absorbance of the two groups.

Western blot

Cells were washed twice with ice-cold PBS and lysed in RIPA buffer supplemented with a protease and phosphatase Inhibitor cocktail (Thermo Fisher). Cell lysates were clarified by centrifugation at 12,000 g for 10 min at 4°C, and protein concentrations were determined using a bicinchoninic acid (BCA) assay (Thermo Fisher). Equivalent amounts of protein were resolved via 4–20% gradient SDS-PAGE (ACE Biotechnology, China) and transferred onto 0.2 μm PVDF membranes (Millipore, USA). Membranes were blocked with 5% non-fat dry milk for 1 h at room temperature, followed by overnight incubation with specific primary antibodies at 4°C. After three washes, membranes were incubated with appropriate horseradish peroxidase (HRP)-conjugated secondary antibodies for 1 h at room temperature. Immunoreactive bands were visualized using an ImageQuan LAS 4000 mini system (Cytiva, USA) following incubation with a chemiluminescent substrate.

Flow cytometry

To minimize non-specific antibody binding, single-cell suspensions were pre-incubated with anti-CD16/CD32 antibody (Biolegend) for 10 min at 4°C. For surface immunostaining, cells were stained with fluorochrome-conjugated antibody panels at 4°C in the dark, adhering to the manufacturer's guidelines. For intracellular cytokine assessment, cells were stimulated in vitro with a Cell Stimulation Cocktail (PMA, ionomycin, monensin, and brefeldin A, Thermo Fisher) for 5 h at 37°C. Following stimulation, cells were subjected to fixation and permeabilization, and subsequently stained with specific anti-cytokine monoclonal antibodies. Data acquisition was performed on a BD FACSymphony A1 (BD Biosciences) or CytoFLEX (Beckman Coulter) flow cytometer. All flow cytometric data were analyzed utilizing FlowJo software (v10.8.1). Detailed antibody information is provided in Supplementary Table S1.

qRT-PCR and ELISA

Total RNA was extracted from cells using TRIzol reagent (Thermo Fisher). Reverse transcription was performed to synthesize cDNA utilizing the Hifair III 1st Strand cDNA Synthesis SuperMix (Yeasen, China). Subsequent qRT-PCR was conducted on a QuantStudio 5 qPCR System (Thermo Fisher) using the Hieff qPCR SYBR Green Master Mix (Yeasen). Relative mRNA expression levels were calculated employing the ΔΔCt method (2-ΔΔCt), with *Gapdh* or *Actb* serving as endogenous controls for normalization. All specific primer sequences are detailed in Supplementary Table S2. Intratumoral levels of ACh and NE were quantified using specific ELISA Kits (mlbio, China) according to the manufacturer's instructions.

Seahorse analysis

Mitochondrial function was evaluated by measuring the oxygen consumption rate (OCR) using a Seahorse XF96 Extracellular Flux Analyzer (Agilent, USA). B cells were seeded into 96-well assay plates at a density of 1×10^5 cells per well. Assays were performed utilizing the Seahorse XF Cell Mito Stress Test Kit (Agilent) according to the manufacturer's instructions. Baseline OCR was recorded, followed by sequential injections of pharmacological modulators: 1 μM oligomycin to inhibit ATP synthase, 2.0 μM FCCP to uncouple mitochondrial oxidative phosphorylation, and a combination of 0.5 μM rotenone and 0.5 μM antimycin A to respectively block electron transport chain complexes I and III.

Coculture of B- and T-cells

Primary bulk B cells and $CD8^+$ T cells were isolated from murine spleens utilizing lineage-

specific negative selection kits (STEMCELL). Prior to co-culture, isolated B cells were pre-stimulated with LPS (10 μg/mL, Sigma-Aldrich), β-ME (50 μM, Sigma-Aldrich), and ACh (50 μM, Sigma-Aldrich) for 24 h. Following the intervention, B cells were extensively washed with PBS to remove all soluble stimuli, including residual ACh. For the indirect co-culture system, pre-conditioned B cells (6×10^5) were seeded into the apical chambers of 24-well Transwell inserts (0.4 μm pore size, Corning), while an equal number (6×10^5) of $CD8^+$ T cells were plated in the basal wells. To induce T cell activation, basal wells were pre-coated with anti-CD3 (5 μg/mL, BioLegend) and anti-CD28 (2 μg/mL, BioLegend), and the culture medium was supplemented with recombinant murine IL-2 (mIL-2, 100 IU/mL, R&D Systems, USA). Additionally, to maintain B cell viability during the co-culture period, LPS (10 μg/mL, Sigma-Aldrich) and β-ME (50 μM, Sigma-Aldrich) were supplemented into the culture system. Cells were co-cultured in a humidified incubator at 37°C with 5% CO_2 for 48 h. For neutralization of IL-10 and TGF-β, B cells were pre-incubated with a neutralizing anti-IL-10 antibody (20 ng/mL, Bio X Cell, USA), anti-TGF-β antibody (20 ng/mL, Bio X Cell), or an isotype-matched control antibody (20 ng/mL, Bio X Cell) for 24 h prior to initiating the co-culture with $CD8^+$ T cells.

In vivo depletion of B cells

Mice were intraperitoneally injected with an anti-CD19 monoclonal antibody (Bio X Cell) or a matched IgG2a isotype control (Bio X Cell). The treatment regimen comprised initial 500 μg doses administered 1 day prior to (day -1) and 2 days post (day +2) MFC cell inoculation, followed by 250 μg maintenance doses every 5 days. Successful systemic B cell depletion was confirmed via flow cytometry.

Quantification and statistical analysis

Statistical analyses were performed using GraphPad Prism 10.5.0 (GraphPad Software). Quantitative data are presented as mean ± standard error of the mean (SEM) unless otherwise specified. For comparisons between two independent groups, an unpaired, two-tailed Student's t-test was utilized. For related groups, a paired, two-tailed Student's t-test was utilized. For comparisons involving multiple groups, one-way or two-way analysis of variance (ANOVA) was applied. Overall survival (OS) and progression-free survival (PFS) analyses were performed using the Kaplan-Meier method, and survival distributions were compared via the log-rank test. Statistical significance was defined as $P < 0.05$. In all figures, significance levels are denoted as follows: * $P < 0.05$; ** $P < 0.01$; *** $P < 0.001$; and ns, not significant.

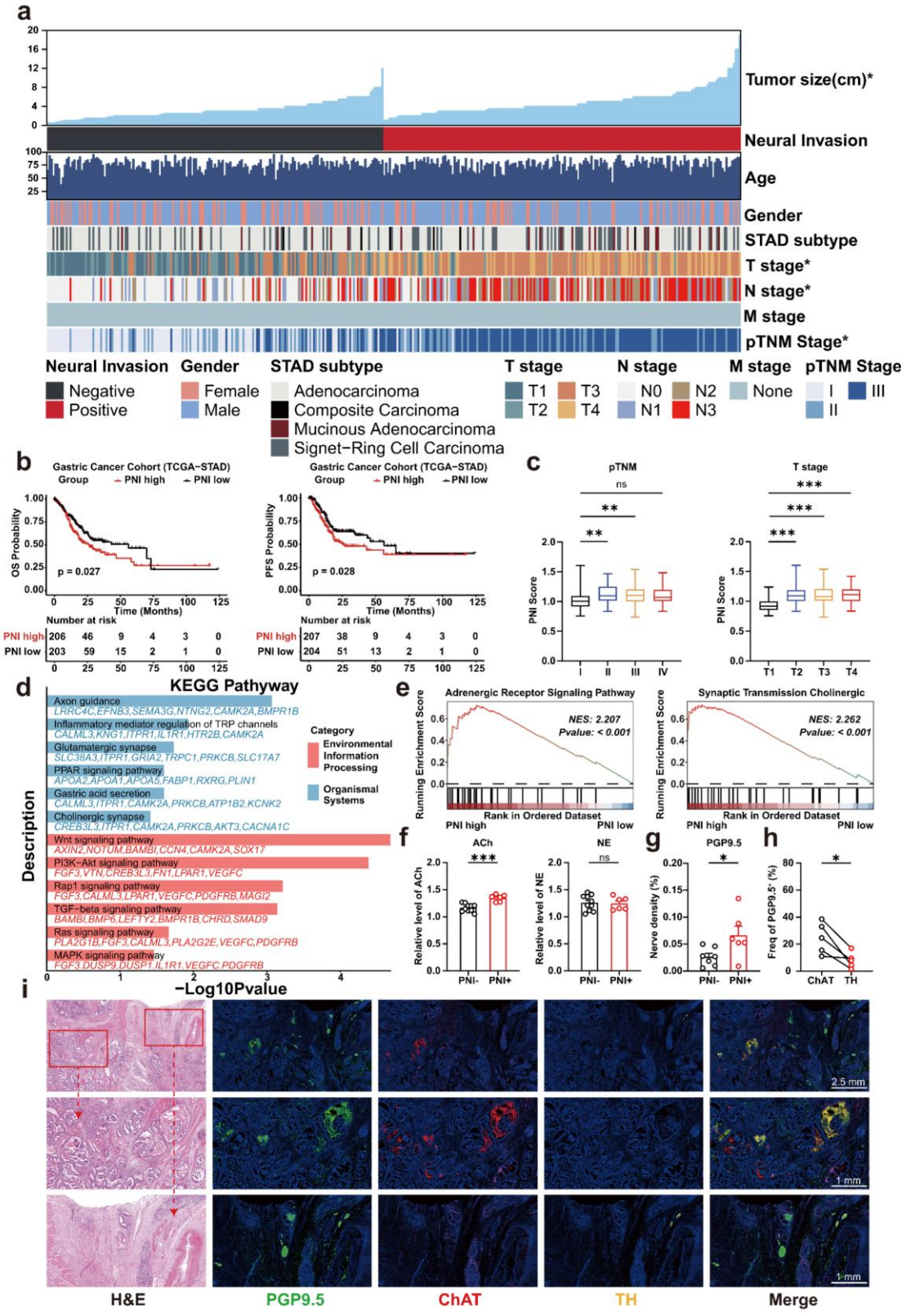


Fig. 1. Perineural invasion correlates with poor prognosis and cholinergic nerve infiltration in gastric cancer.

(**a**) Association of perineural invasion (PNI) status with clinicopathological characteristics in the Huashan Hospital gastric cancer (GC) cohort (*n* = 365 independent patients). Variables include tumor size, age, sex, pathological subtype of stomach adenocarcinoma (STAD), primary tumor stage, regional lymph node involvement, distant metastasis, and pathological tumor node metastasis (pTNM) stage.

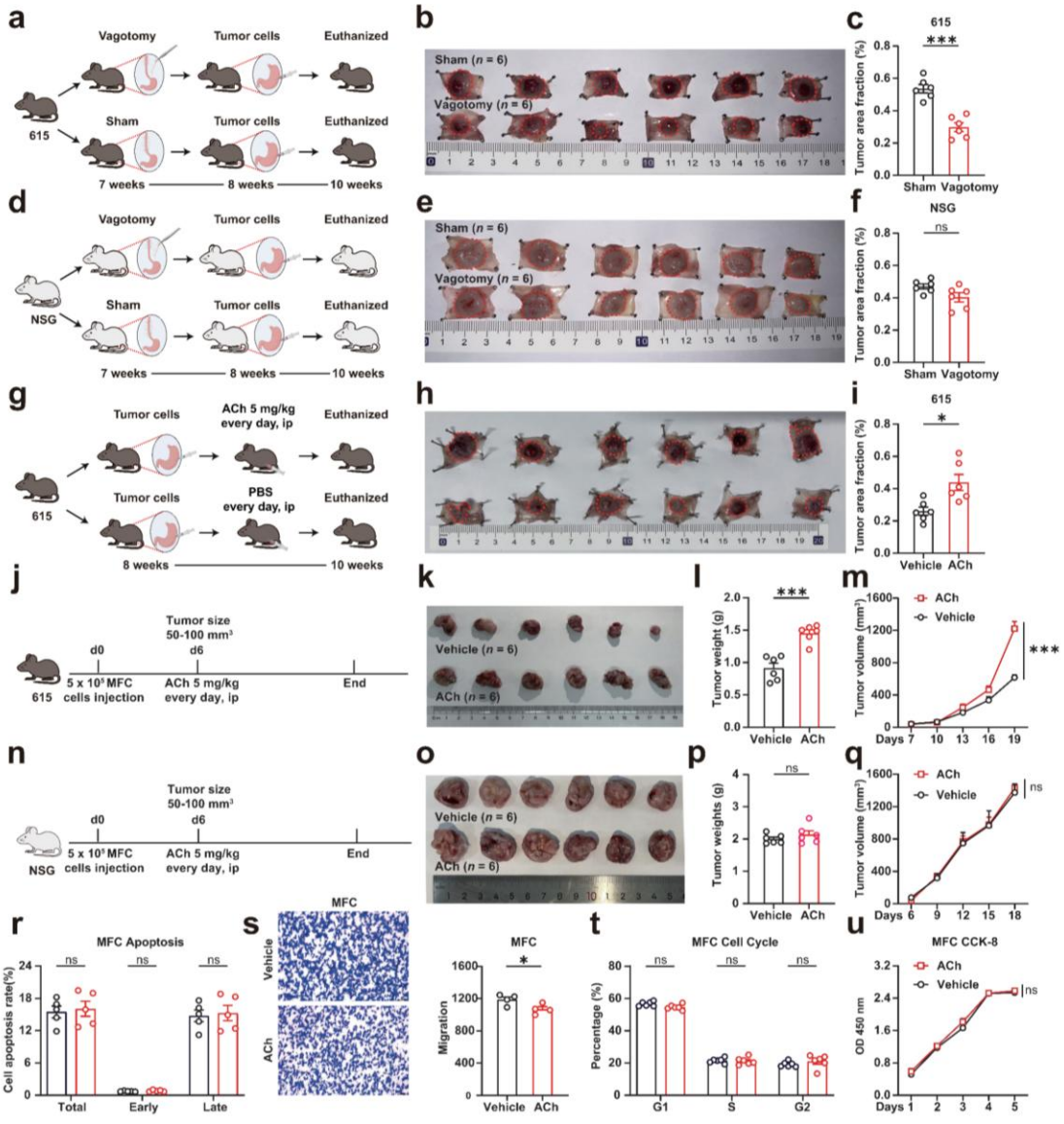
(**b-e**) Transcriptomic profiling of the TCGA-STAD dataset based on PNI scores derived from an established PNI-associated gene signature. Kaplan–Meier survival curves for overall survival (**b, *left***) and progression-free survival (**b, *right***) of patients with GC stratified into PNI-high and PNI-low groups by the median PNI score (**b**); correlation between PNI scores and clinical tumor stages (**c**); KEGG pathway enrichment analysis revealing differentially activated pathways between PNI-high and PNI-low tumors (**d**); gene set enrichment analysis (GSEA) of the indicated pathways in PNI-high versus PNI-low tumors (**e**).

(**f**) Relative concentrations of acetylcholine (ACh) and norepinephrine (NE) in fresh PNI-positive (*n* = 6 patients) and PNI-negative (*n* = 10 patients) GC tissues determined by ELISA.

(**g**) Quantification of PGP9.5$^+$ nerve density in human GC tissues with (PNI-positive, *n* = 6 patients) or without (PNI-negative, *n* = 7 patients) PNI.

(**h-i**) Characterization of nerve fiber subtypes in human GC tissues (*n* = 5). Corresponding quantification of PGP9.5$^+$ ChAT$^+$ and PGP9.5$^+$ TH$^+$ nerve densities (**h**); Representative multiplex immunofluorescence (mIF) images stained for PGP9.5 (pan-neuronal), ChAT (cholinergic), and TH (adrenergic) markers. Scale bars, 2.5 mm; magnified inset, 1 mm (**i**).

Statistical significance was calculated by Fisher's exact test (**a**), unpaired two-tailed Student's t tests (**f, g**), paired two-tailed Student's t tests (**h**), one-way ANOVA (**c**), and log-rank test (**b**). Error bars represent SEM. * $P < 0.05$, ** $P < 0.01$, *** $P < 0.001$, and ns, not significant.



741

742 **Fig. 2. Cholinergic signaling promotes gastric cancer progression via an immune-**
743 **dependent mechanism.**

744 (**a–c**) Effect of surgical denervation on tumor growth in immunocompetent mice.
745 Subdiaphragmatic vagotomy or sham surgery was performed on syngeneic 615 mice,
746 followed by orthotopic implantation of murine forestomach carcinoma (MFC) cells (n = 6
747 mice per group). Experimental workflow (**a**); photographs of tumors (**b**); quantification of
748 tumor area fraction (calculated as tumor area divided by total gastric area) (**c**).

749 (**d–f**) Effect of surgical denervation on tumor growth in immunodeficient mice.

Subdiaphragmatic vagotomy or sham surgery was performed on immunodeficient NSG mice, followed by orthotopic implantation of MFC cells (n = 6 mice per group). Experimental workflow (**d**); photographs of tumors (**e**); quantification of tumor area fraction (calculated as tumor area divided by total gastric area (**f**).

(**g–i**) Effect of exogenous ACh treatment on orthotopic gastric tumor growth in immunocompetent mice (n = 6 mice per group). Experimental workflow (**g**); photographs of tumors (**h**); quantification of tumor area fraction (calculated as tumor area divided by total gastric area) (**i**).

(**j–m**) *In vivo* evaluation of exogenous ACh treatment in the MFC syngeneic model (615 mice, n = 6 mice per group). Experimental workflow (**j**); photographs of tumors (**k**); final weights of tumors (**l**) and tumor growth curves (**m**).

(**n–q**) *In vivo* evaluation of exogenous ACh treatment in the MFC immunodeficient model (NSG mice, n = 6 mice per group). Experimental workflow (**n**); photographs of tumors (**o**); final weights of tumors (**p**) and tumor growth curves (**q**).

(**r–u**) *In vitro* assays of MFC cells following ACh treatment (n = 4–6). Apoptosis assay (**r**); migration assay (**s**); cell cycle assay (**t**); CCK-8 cell viability assay (**u**).

Statistical significance was calculated by unpaired two-tailed Student's t tests (**c, f, i, l, p, s**), one-way ANOVA (**r, t**) and two-way ANOVA (**m, q, u**). Error bars represent SEM. * P < 0.05, ** P < 0.01, *** P < 0.001, and ns, not significant.

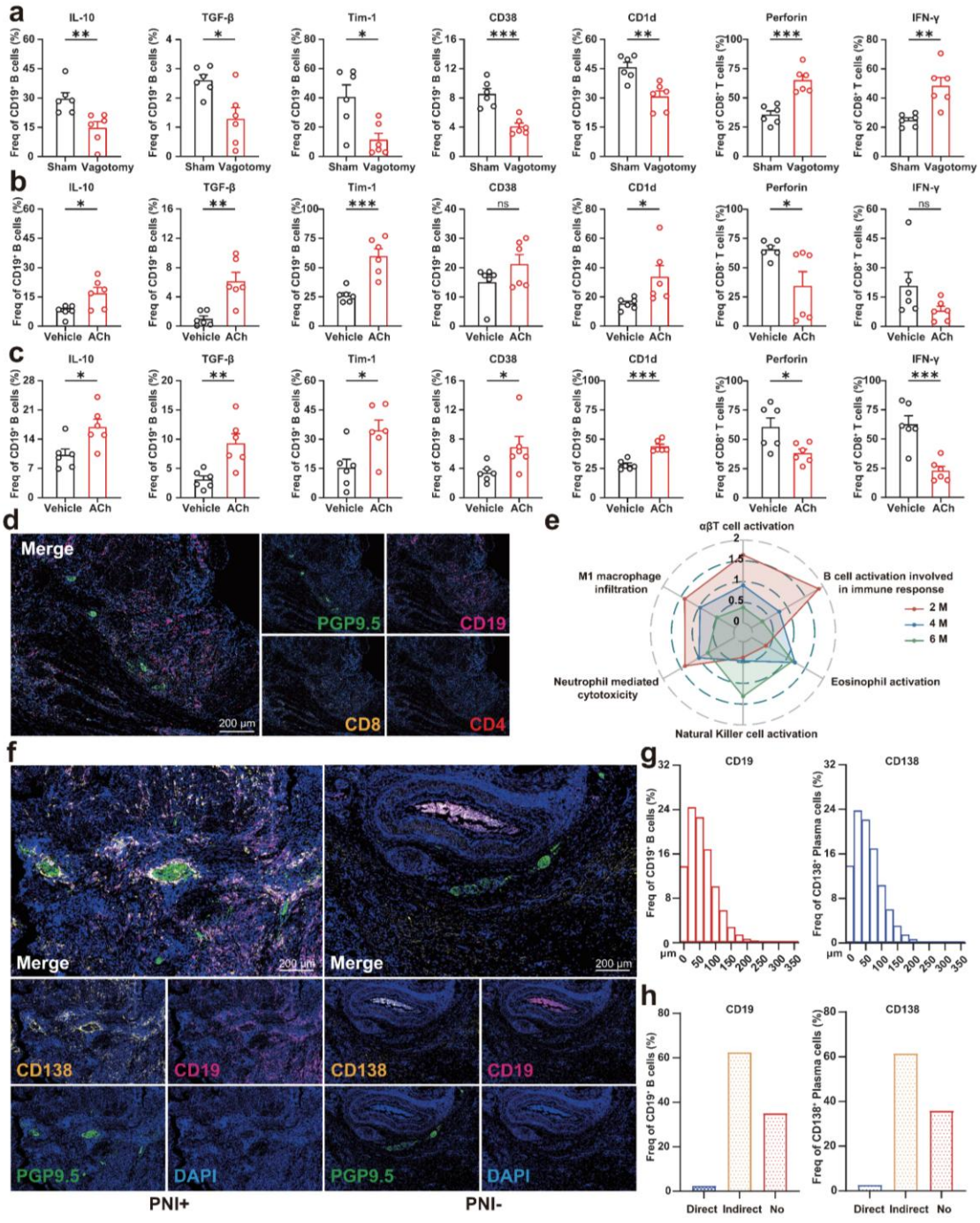


Fig. 3. Cholinergic signaling shapes the immunosuppressive landscape of the tumor microenvironment.

(**a–c**) Flow cytometric quantification of immunosuppressive and effector immune cell subpopulations in murine tumor models (n = 6 mice per group). Proportions of IL-10$^+$, TGF-β$^+$, Tim-1$^+$, CD38$^+$, and CD1d$^+$ cells among CD19$^+$ B cells, alongside perforin$^+$ and IFN-γ$^+$ cells among CD8$^+$ T cells, were quantified in an orthotopic tumor model comparing sham-

operated versus vagotomized mice (**a**), and PBS- versus ACh-treated mice (**b**); corresponding flow cytometric quantification in a subcutaneous tumor model treated with PBS or ACh (**c**).

(**d**) Representative immunofluorescence images of $CD8^+$ T cells, $CD4^+$ T cells and $CD19^+$ B cells infiltrating the perineural niche of human GC tissues (scale bar = 200 μm).

(**e**) Time-course enrichment of six key signaling pathways determined by microarray analysis in the anterior side of the stomach at 2 (red), 4 (blue), and 6 (green) months after anterior unilateral vagotomy compared with the posterior side of the stomach in INS-GAS mice.

(**f**) Representative immunofluorescence images of $CD138^+$ plasma cells and $CD19^+$ B cells infiltrating the perineural niche of human GC tissues (scale bar = 200 μm).

(**g**) Morphometric quantification of nerve–B cell spatial distances.

(**h**) Stratification of nerve–B cell proximity based on inferred spatial interaction modes, categorized as "direct" (cell-to-cell contact, <10 μm), "indirect" (paracrine signaling via cytokines or neurotransmitters, 10–80 μm), and "no" interaction (>80 μm).

Statistical significance was calculated by unpaired two-tailed Student's t tests (**a, b, c**). Error bars represent SEM. * $P < 0.05$, ** $P < 0.01$, *** $P < 0.001$, and ns, not significant.

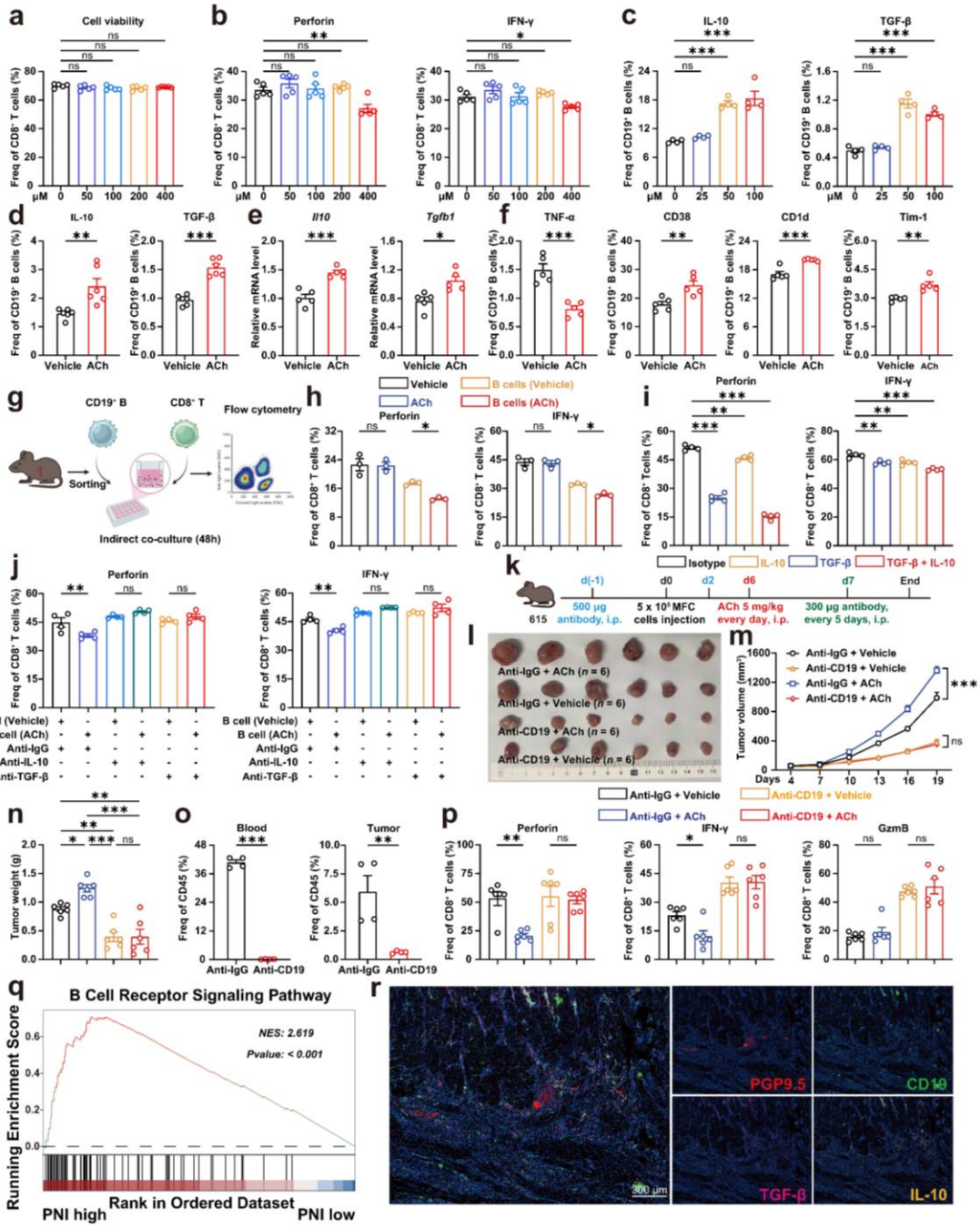


Fig. 4. B cell-derived IL-10 and TGF-β mediate cholinergic suppression of CD8⁺ T cell anti-tumor immunity.

(**a–b**) In vitro phenotypic and functional evaluation of murine CD8⁺ T cells following a 24-h exposure to indicated concentrations of ACh or PBS (*n* = 5). Flow cytometric assessment of cell viability (**a**); intracellular flow cytometric quantification of the effector molecules perforin and IFN-γ (**b**).

(**c**) Proportion of murine CD19$^+$ B cells expressing cytokines (IL-10, TGF-β) upon T cell-independent activation, followed by a 24-h treatment with varying doses of ACh or PBS (*n* = 4).

(**d**) Proportion of murine CD19$^+$ B cells expressing cytokines (IL-10, TGF-β) upon T cell-dependent activation, followed by a 24-h treatment with 50 μM ACh or PBS (*n* = 6).

(**e**) Relative mRNA expression levels of *Il10* and *Tgfb1* in murine B cells treated with 50 μM ACh or PBS for 24 h, determined by qRT-PCR (*n* = 5).

(**f**) Flow cytometric analysis of TNF-α expression and regulatory B cell (Breg)-associated surface markers (CD38, CD1d, and Tim-1) on murine B cells treated with 50 μM ACh or PBS for 24 h (*n* = 5).

(**g–h**) *In vitro* indirect co-culture of B cells and CD8$^+$ T cells sorted from murine spleens (*n* = 3). Schematic illustration of the indirect co-culture experimental design (**g**); flow cytometric evaluation of CD8$^+$ T cell effector function following indirect co-culture with B cells pre-treated with 50 μM ACh or PBS (**h**).

(**i**) Proportion of murine CD8$^+$ T cells expressing effector molecules (perforin, IFN-γ) after a 24-h treatment with IL-10 and/or TGF-β (alone or in combination) (*n* = 4).

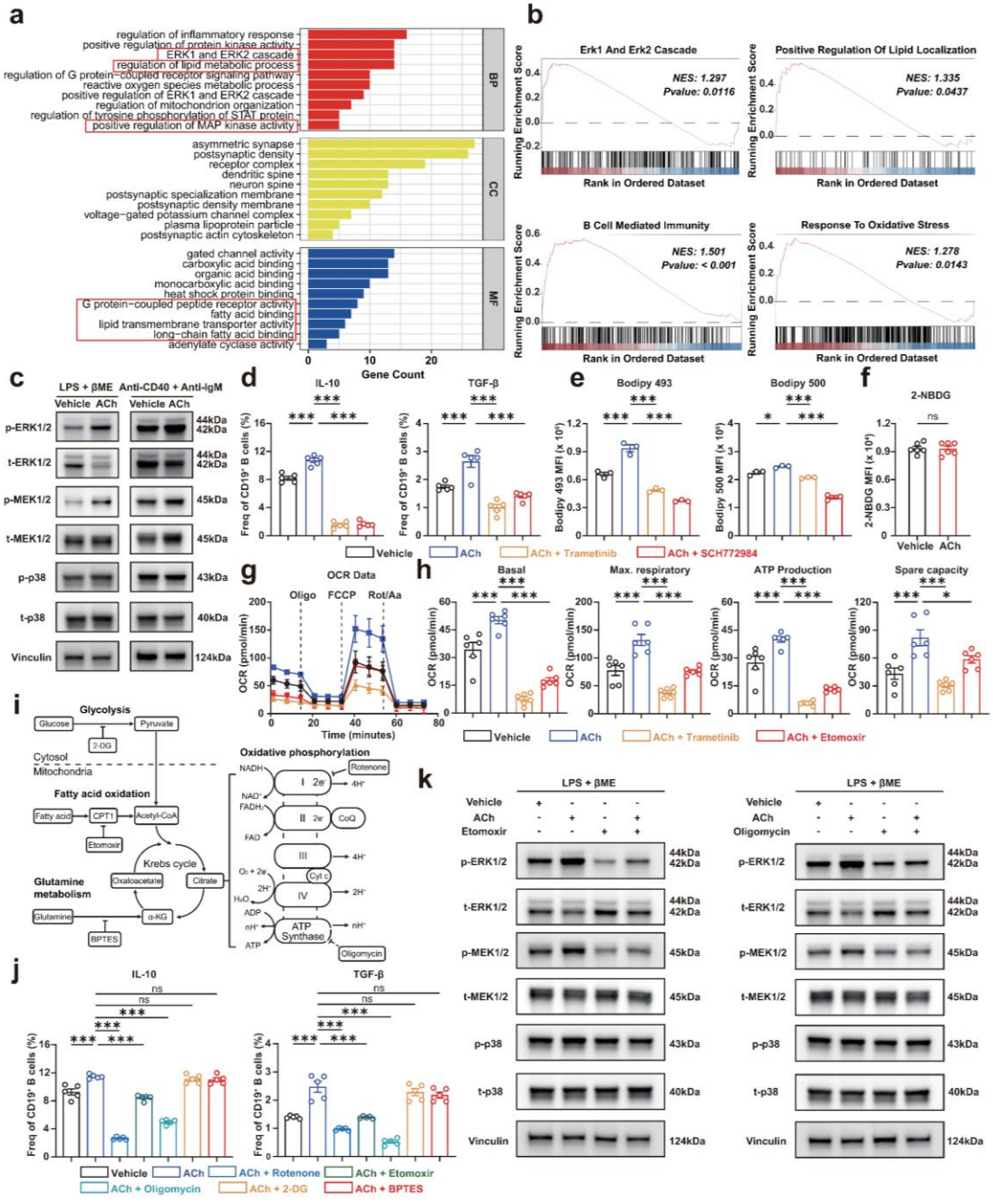
(**j**) Flow cytometric analysis of murine CD8$^+$ T cell function following indirect co-culture with ACh- or PBS-pre-treated murine B cells in the presence or absence of neutralizing antibodies against IL-10 and TGF-β (*n* = 4).

(**k–p**) *In vivo* evaluation of ACh treatment in the MFC syngeneic tumor model (615 mice) with anti-CD19 antibody-mediated B cell depletion (*n* = 6 mice per group). Experimental workflow (**k**); photographs of tumors (**l**); tumor growth curves (**m**); final weights of tumors (**n**); depletion efficiency of CD19$^+$ B cells in peripheral blood (**o, *left***) and tumor (**o, *right***) tissues; proportions of perforin$^+$ CD8$^+$ T, IFN-γ$^+$ CD8$^+$ T and GzmB$^+$ CD8$^+$ T cells among tumor-infiltrating CD8$^+$ T cells (**p**).

(**q**) Transcriptomic profiling of the TCGA-STAD dataset based on PNI scores derived from an established PNI-associated gene signature. GSEA evaluates the enrichment of indicated pathways between the PNI-high and PNI-low groups.

(**r**) Representative immunofluorescence images showing co-localization of $CD19^+$ B cells with IL-10 and TGF-β within the perineural niche of human GC tissues (scale bar = 300 μm).

Statistical significance was calculated by unpaired two-tailed Student's t tests (**d, e, f, o**), one-way ANOVA (**a, b, c, h, i, j, n, p**) and two-way ANOVA (**m**). Error bars represent SEM. * $P < 0.05$, ** $P < 0.01$, *** $P < 0.001$, and ns, not significant.



834

835 **Fig. 5. Acetylcholine drives an immunosuppressive B cell phenotype via a**

836 **MEK/ERK-dependent lipid-OXPHOS metabolic axis.**

837 (**a–b**) Transcriptomic analysis of murine B cells treated with ACh or PBS (*n* = 3 biological

838 replicates). Gene Ontology (GO) terms enriched in ACh-treated CD19^{+} B cells, based on

839 bulk RNA-seq data (**a**); enrichment of indicated pathways in ACh- or PBS-treated group,

840 determined by GSEA (**b**).

(**c**) Immunoblots for indicated proteins of whole-cell lysates from murine B cells subjected to T cell-independent or T cell-dependent activation with treatment as indicated.

(**d**) Murine B cells were pretreated with or without MEK/ERK inhibitors trametinib (10 μM) or SCH772984 (10 μM) for 30 min, and then stimulated with or without 50 μM ACh. After an additional 24 h, the proportion of IL-10- and TGF-β-producing $CD19^+$ B cells was determined by flow cytometry (*n* = 5).

(**e**) Murine B cells were pretreated with or without MEK/ERK inhibitors trametinib (10 μM) or SCH772984 (10 μM) for 30 min, and then stimulated with or without 50 μM ACh. After an additional 24 h, the lipid uptake and lipid content in B cells was determined by flow cytometry (*n* = 3).

(**f**) Flow cytometric analysis of glucose uptake using 2-NBDG staining in murine B cells treated with ACh or PBS (*n* = 6).

(**g–h**) Oxygen consumption rate (OCR) assay of murine B cells following the indicated treatments (*n* = 6). Real-time OCR was measured at baseline and in response to oligomycin, FCCP, and rotenone/antimycin A (**g**); Basal, Max.respiratory, ATP Production, and Spare capacity are shown (**h**).

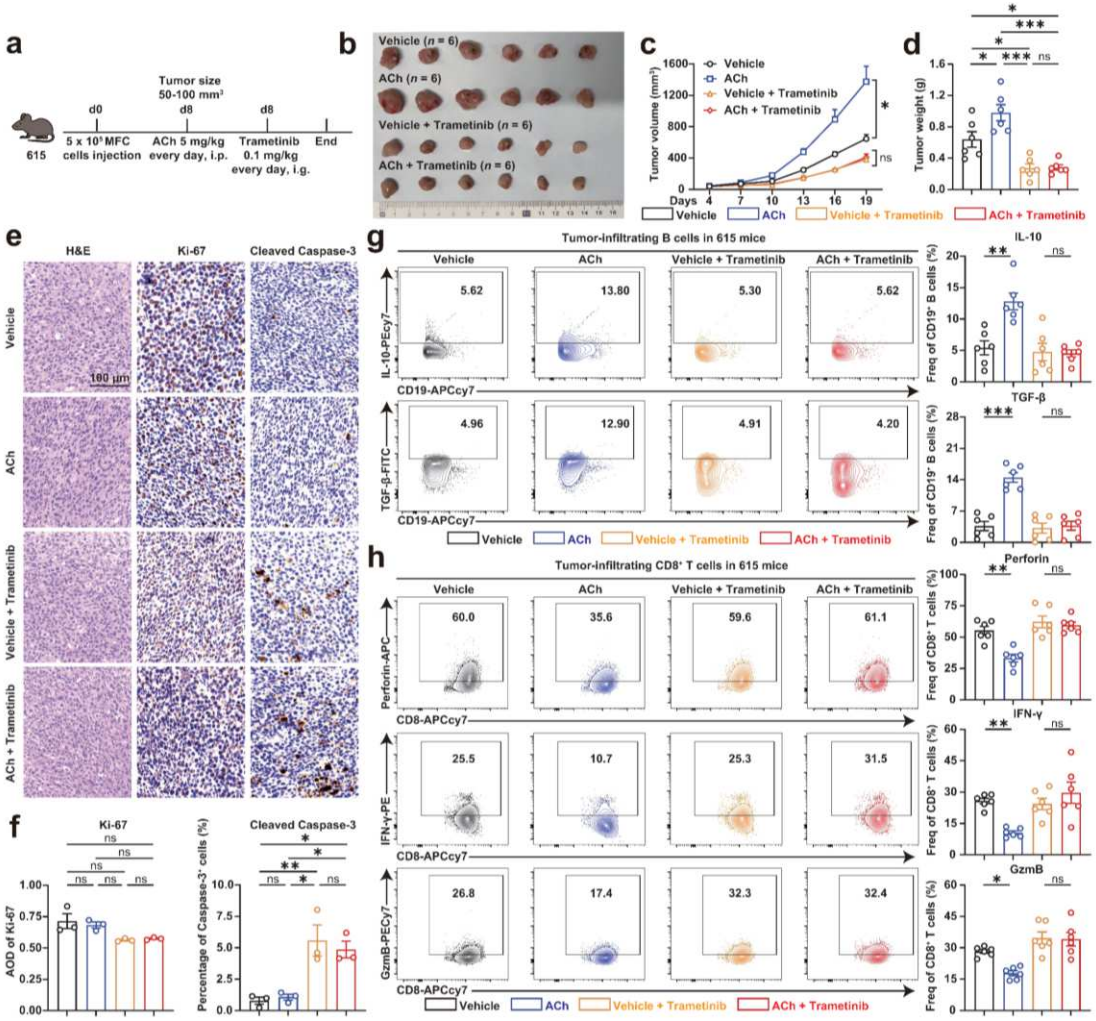
(**i**) Schematic overview of key cellular metabolic pathways and their respective pharmacological inhibitors: 2-DG (glycolysis), etomoxir (fatty acid oxidation), BPTES (glutamine metabolism), rotenone (electron transport chain complex I), and oligomycin (ATP synthase).

(**j**) Flow cytometric analysis of IL-10 and TGF-β production in murine $CD19^+$ B cells. Cells were stimulated with LPS for 24 h and subsequently treated with 50 μM ACh, either alone or in combination with specific metabolic inhibitors (1 mM 2-DG, 20 μM etomoxir, 0.1 μM rotenone, 0.1 μM BPTES, or 0.1 μM oligomycin) (*n* = 5).

(**k**) Immunoblots for indicated proteins of whole-cell lysates from murine B cells with

866 treatment as indicated.

867 Statistical significance was calculated by unpaired two-tailed Student's t tests (**f**), one-way
868 ANOVA (**d, e, h, j**). Error bars represent SEM. * $P < 0.05$, ** $P < 0.01$, *** $P < 0.001$, and
869 ns, not significant.



870

871 **Fig. 6. Targeting the MEK/ERK axis curtails tumor progression via immune**
872 **remodeling and direct induction of apoptosis.**

873 (**a–h**) *In vivo* evaluation of ACh or PBS treatment combined with the MEK inhibitor
874 trametinib in the MFC syngeneic tumor model (615 mice, *n* = 6 mice per group).
875 Experimental workflow (**a**); photographs of tumors (**b**); tumor growth curves (**c**); final
876 weights of tumors (**d**); representative H&E staining and immunohistochemistry (IHC)
877 images of Ki-67 and Cleaved Caspase-3 in tumor sections from the indicated groups (**e**);
878 corresponding quantification of Ki-67 and Cleaved Caspase-3 (**f**); proportion of TGF-β$^+$ and
879 IL-10$^+$ cells among tumor-infiltrating CD19$^+$ B cells, determined by flow cytometry (**g**);
880 proportion of perforin$^+$, IFN-γ$^+$, and GzmB$^+$ cells among tumor-infiltrating CD8$^+$ T cells (**h**).

881 Statistical significance was calculated by one-way ANOVA (**d, f, g, h**) and two-way ANOVA

882 (**c**). Error bars represent SEM. * $P < 0.05$, ** $P < 0.01$, *** $P < 0.001$, and ns, not significant.

Supplementary Files

This is a list of supplementary files associated with this preprint. Click to download.

- SupplementaryTableS2.xlsx
- Table1.xlsx
- SupplementaryTableS1.xlsx
- Supplementarydata.pdf